Evaluation of EarthCARE Cloud Profiling Radar Doppler Velocity Measurements in Particle Sedimentation Regimes

PAVLOS KOLLIAS

Department of Atmospheric and Oceanic Sciences, McGill University, Montreal, Quebec, Canada

SIMONE TANELLI

Jet Propulsion Laboratory, California Institute of Technology, Pasadena, California

ALESSANDRO BATTAGLIA

Department of Physics and Astronomy, University of Leicester, Leicester, United Kingdom, and Meteorological Institute, University of Bonn, Bonn, Germany

ALEKSANDRA TATAREVIC

Department of Atmospheric and Oceanic Sciences, McGill University, Montreal, Quebec, Canada

ABSTRACT

The joint European Space Agency–Japan Aerospace Exploration Agency (ESA–JAXA) Earth Clouds, Aerosols and Radiation Explorer (EarthCARE) mission is scheduled for launch in 2016 and features the first atmospheric Cloud Profiling Radar (CPR) with Doppler capability in space. Here, the uncertainty of the CPR Doppler velocity measurements in cirrus clouds and large-scale precipitation areas is discussed. These regimes are characterized by weak vertical motion and relatively horizontally homogeneous conditions and thus represent optimum conditions for acquiring high-quality CPR Doppler measurements. A large dataset of radar reflectivity observations from ground-based radars is used to examine the homogeneity of the cloud fields at the horizontal scales of interest. In addition, a CPR instrument model that uses as input ground-based radar observations and outputs simulations of CPR Doppler measurements is described. The simulator accurately accounts for the beam geometry, nonuniform beam-filling, and signal integration effects, and it is applied to representative cases of cirrus cloud and stratiform precipitation. The simulated CPR Doppler velocities are compared against those derived from the ground-based radars. The unfolding of the CPR Doppler velocity is achieved using simple conditional rules and a smoothness requirement for the CPR Doppler measurements. The application of nonuniform beam-filling Doppler velocity bias-correction algorithms is found necessary even under these optimum conditions to reduce the CPR Doppler biases. Finally, the analysis indicates that a minimum along-track integration of 5000 m is needed to reduce the uncertainty in the CPR Doppler measurements to below $0.5\,\mathrm{m\,s^{-1}}$ and thus enable the detection of the melting layer and the characterization of the rain- and ice-layer Doppler velocities.

1. Introduction

The Earth Clouds, Aerosols and Radiation Explorer (EarthCARE; EarthCARE 2004) satellite is a joint European Space Agency (ESA) and Japanese Aerospace Exploration Agency (JAXA) mission, and is scheduled for launch in 2016. EarthCARE (EC) aims at a better understanding of the interactions between cloud, radiative, and aerosol processes that play a role in climate regulation, and it includes a spaceborne 94-GHz Doppler Cloud Profiling Radar (EC-CPR). The EC-CPR will be the first spaceborne Doppler cloud radar used in climate research and evaluation of numerical weather prediction models (e.g., Kobayashi et al. 2002): its Doppler capability along with its high sensitivity ($-35\,\mathrm{dB}Z$ or better) is a step forward in spaceborne

Corresponding author address: Pavlos Kollias, Department of Atmospheric and Oceanic Sciences, McGill University, Room 945, Burnside Hall, 805 Sherbrooke Street West, Montreal QC H3A 0B9, Canada.
E-mail: pavlos.kollias@mcgill.ca

millimeter-wave radars beyond the current state-of-the-art defined by the CPR on *CloudSat*, a joint National Aeronautics and Space Administration (NASA) and Canadian Space Agency (CSA) mission (e.g., Stephens et al. 2008).

The availability of Doppler measurements from space will offer a unique opportunity for the collection of a global dataset of vertical motions in clouds and precipitation. Such a global dataset is expected to improve our understanding of convective motions in clouds and to help evaluate current parameterizations of convective mass flux in cloud-resolving models (e.g., Manabe and Strickler 1964; Tiedtke 1989; Bechtold et al. 2001). Furthermore, global climate models (GCMs) required an accurate representation of ice particle sedimentation rates (e.g., Mitchell et al. 2008; Sanderson et al. 2008), which the CPR Doppler measurements can potentially provide. The Doppler measurements from space will also help to constrain the retrieval of particles' characteristic size in drizzling and large-scale precipitation conditions. Notably, Doppler capability has been recognized as a critical capability not only by ESA and JAXA but also by the U.S. National Research Council (in its decadal survey; National Research Council 2007) for a radar system on board the NASA Aerosol Cloud Ecosystems (ACE) mission and other mission concepts, and by the Canadian proposed concepts of SnowSat and Polar Precipitation Measurement mission (PPM; Joe et al. 2010; Kollias et al. 2007b).

Early detailed studies of Doppler measurements with spaceborne radars articulate the challenges in developing Doppler capability for atmospheric research from space due to the platform motion and second-trip echoes (Lhermitte 1989; Amayenc et al. 1993; Meneghini and Kozu 1990). Several of the aforementioned challenges can be theoretically mitigated using sophisticated transmit waveforms with variable pulse length and polarization diversity. The planned EC-CPR uses a simple short single-pulse (i.e., narrowband, single carrier) transmit waveform with no frequency modulation or polarization diversity. Thus, the EC-CPR Doppler performance is challenged by the fundamental constrains of Doppler measurements from space in its chosen configuration (Kobayashi et al. 2002). The main challenge in spaceborne Doppler measurements from low-Earth-orbiting (LEO) satellites arises from their high relative speed ($V_{sat} \sim 7.6 \text{ km s}^{-1}$) that introduces significant broadening of the Doppler spectrum, even if the radar is pointing perfectly perpendicular to its motion. Doppler velocity aliasing, cloud inhomogeneity (Tanelli et al. 2002a,b; Schutgens 2008), multiple scattering (Battaglia et al. 2010, 2011), and pointing uncertainty (Tanelli et al. 2005) are additional sources of error and uncertainty in Doppler moment estimation from space.

Here, the expected uncertainty in EC-CPR Doppler velocity measurements in nonconvective conditions is investigated using an EC-CPR Doppler velocity simulator that uses as input ground-based radar data. The simulator and a comprehensive analysis of the critical parameters that affect the performance of EC-CPR Doppler measurements from space are presented in section 2. A detailed climatology of radar reflectivity variability in clouds and precipitation in several different climatological regimes is used to assess the along-track variability of clouds and precipitation (section 3). Illustrative applications of the EC-CPR simulator to a cirrus cloud and a stratiform precipitation case, and a quantitative comparison of the observed and simulated Doppler velocities are discussed in section 4.

2. Background

a. Challenges associated with EC-CPR Doppler measurements

In contrast to radar power estimates (e.g., radar reflectivity), Doppler velocity estimation requires coherent measurements of phase changes between successive radar returns. In general, this requires such returns to be acquired with an intrapulse period (IPP) significantly shorter than the decorrelation time. When the pulses are transmitted with a constant IPP, it is customary to adopt its inverse (pulse repetition frequency, PRF = 1/IPP) to indicate the timing configuration. A parameter that is indicative of the signal correlation is the normalized Doppler spectrum width σ_f/PRF, where $\sigma_f = \sigma_v /(\lambda/2)$, λ is the radar wavelength, and σ_v is the Doppler velocity spectral width, which for space-based profiling radars (narrow beam) can be expressed in first approximation as the sum of several independent sources of Gaussian spreading:

$$\sigma_v^2 = \sigma_{SM}^2 + \sigma_{PSD}^2 + \sigma_T^2 + \sigma_{WS}^2, \qquad (1)$$

where σ_{SM} is the spread due to the satellite motion, given, for circular antenna patterns, by $\sigma_{SM} \approx 0.3 V_{sat}\theta_{3dB}$ (Sloss and Atlas 1968) and V_{sat} is the satellite velocity; and θ_{3dB} is the 3-dB beamwidth of the antenna in radians that depends on the antenna size ($\theta_{3dB} \sim 1.2\lambda/D_A$ for a typical parabolic antenna), where D_A is the antenna diameter. The other three terms—σ_{PSD} is broadening due to the particle fall velocities, σ_T is broadening due to turbulence at scales smaller than the radar sampling volume, and σ_{WS} is broadening due to wind shear within the radar sampling volume—depend on the cloud and precipitation microphysics and dynamics, and their value depends on the dimensions of the radar pulse. The σ_{PSD}

term ranges from a few $cm\,s^{-1}$ for cloud droplets and ice crystals to 1.0–$2.5\,m\,s^{-1}$ for raindrop size distributions; thus, it is not negligible in rainfall. In moderate turbulence and wind shear regimes, the wind shear and turbulence terms can be as high as $1\,m\,s^{-1}$ and thus should, in general, not be ignored. Nevertheless, for simplicity, it is assumed for the moment that the first term dominates the spread of the velocities for typical radars in LEO ($\sigma_v^2 \approx \sigma_{SM}^2$). The acquisition of coherent samples for reliable Doppler estimates requires that the radar samples be collected at sufficiently high PRF. A constraint traditionally adopted in ground-based Doppler weather radars is (Doviak and Zrnić 1993)

$$\mathrm{PRF} \ge \frac{4\pi\sigma_V}{\lambda}, \qquad (2)$$

which for LEO and narrow beamwidth (i.e., under the $\sigma_v^2 \approx \sigma_{SM}^2$ assumption) becomes

$$\frac{\mathrm{PRF}}{\theta_{3dB}} \ge \frac{1.2\pi V_{sat}}{\lambda}. \qquad (3)$$

Given the EC-CPR θ_{3dB} (0.095° based on actual measurements of the 2.5-m-diameter CPR), the range of selected operational PRF (6.1–7.5 kHz, variable within each orbit with the platform latitude) is well below the required value (14 kHz) to satisfy the criteria for sample coherency (for EC-CPR, the $\sigma_{SM} \approx 3.8\,m\,s^{-1}$). The upper-bound limit of 7.5 kHz (22.5-km unambiguous range) is imposed by the constraint to observe the entire troposphere without second-trip ambiguous overlaps, and this creates an inconvenient truth for the EC-CPR. Furthermore, the high velocity of LEO platforms usually imposes short integration times to preserve along-track resolution: in the case of EC-CPR, the integration time for level 0 products is set to approximately 65 ms (resulting in a 500-m along-track sampling). Longer integration times can be used in ground processing to reduce the variance of the Doppler velocity estimates. For reference, with a PRF of 7 kHz and a $V_{sat} = 7.6\,km\,s^{-1}$, the EC-CPR can collect up to 460 samples every 500 m (in practice, about 10% of said samples are traded to obtain background noise estimates instead). Furthermore, given the parameters mentioned above, the EC-CPR range of Nyquist velocities ($V_N = \lambda \times \mathrm{PRF}/4$) ranges from $V_N = \pm4.9$ to $\pm6.0\,m\,s^{-1}$. Using these two sets of parameters, radar signal simulations were performed (Fig. 1) to assess the EC-CPR Doppler velocity variance for a wide range of along-track integrations (500, 1000, 2500, and 5000 m) and signal-to-noise ratio (SNR) conditions [-20 to $+30$ on a logarithmic scale (dB)]. For each set of conditions, a large number (i.e.,
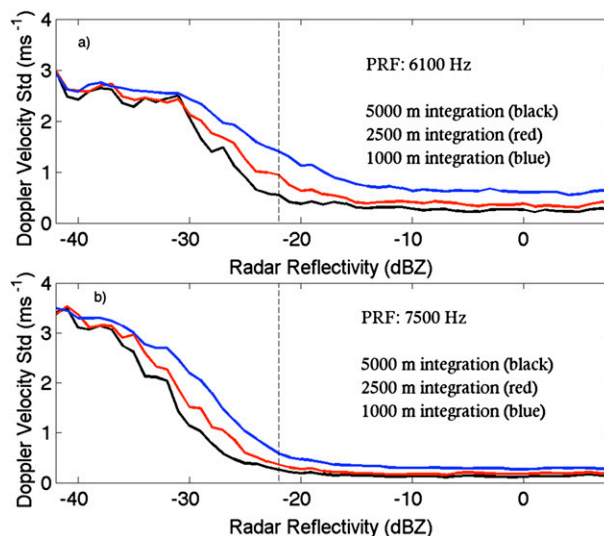

FIG. 1. Standard deviation of the EC-CPR Doppler velocity estimates as a function of radar reflectivity and signal integration conditions. Two PRF settings are considered: (a) 6100 and (b) 7500 Hz. Three different integration lengths are considered: 1000 (blue), 2500 (red) and 5000 m (black). Each point in the figure corresponds to the standard deviation of the estimate from 10 000 realizations using the same SNR and signal integration conditions. Radar reflectivities below $-21.5\,dBZ$ (vertical black line) correspond to negative SNR conditions. SNR is defined on a logarithmic scale.

1000) of radar Doppler spectra centered on zero velocity are generated as in Zrnić (1975). The assumption of zero mean Doppler velocity implies still hydrometeors (i.e., the hydrometeors have either negligible fall velocity or it is balanced by an updraft) in the radar sampling volume, and it is used to study the best-case scenario and isolate the effect of signal decorrelation on the quality of the CPR Doppler measurements (Tanelli et al. 2002a,b). The resulting Doppler spectra are then inverted (Zrnić 1975) and the in-phase and quadrature components (I/Q) of the radar echo of various lengths are input to autocovariance analysis by means of the pulse-pair (PP) processing technique for the estimation of the Doppler velocity (Zrnić 1977). A cloud with radar reflectivity of $-21.5\,dBZ$ generates a radar return power that is approximately equal to the EC-CPR receiver noise ($\mathrm{SNR} = 0$ dB—that is, signal power equals the receiver noise power) for a single pulse (Fig. 1, black vertical line). For very low SNR, the standard deviation of the radar Doppler spectrum reaches the limit value for a white noise power spectrum ($2V_N/\sqrt{12} = 2.82$ and $3.46\,m\,s^{-1}$ for Figs. 1a and 1b, respectively).

At low SNR conditions ($\mathrm{SNR} < 0$, left of the vertical black line in Fig. 1), the standard deviation of the Doppler velocity is high and makes its application challenging. For the EC-CPR, such low SNR conditions

will be observed in liquid clouds and thin ice clouds or near the tops of thicker cirrus clouds. The small hydrometeors contained in these clouds have negligible fall velocities, and the observed Doppler velocity is dominated by cloud turbulence and gravity waves (e.g., Kollias et al. 2001). Even if we could observe their Doppler velocity with sufficient accuracy, it will contain little or no information of characteristic particle size. Furthermore, the size of the EC-CPR footprint (700 m along track and 500 m vertical) will average out all small-scale turbulence information. Thus, it is suggested that CPR Doppler velocities recorded in cloud layers with low radar reflectivity (e.g., below $-20\,dBZ$) will be classified as unrecoverable and thus will be filtered out of final CPR Doppler velocity products. The lack of CPR Doppler velocity measurements in cloud-only systems will have a very small impact on the EC mission scientific objectives.

At higher SNR conditions (SNR $>$ 0, right of the vertical black line in Fig. 1), the theoretical limit of the standard deviation of the Doppler velocity is above $1\,m\,s^{-1}$ for 1000-m integration for radar reflectivities below $-15\,dBZ$ for the low PRF option. For the high PRF setting, the standard deviation for 1000-m integration is below $1\,m\,s^{-1}$ for positive SNR values. Furthermore, the standard deviation is inversely proportional to the square root of the along-track integration. The required reduction in the standard deviation of the Doppler velocity depends on the scientific application and this dictates the length of the along-track integration in particle sedimentation regimes. In the case of large ice crystals or drizzle particles, the observed Doppler velocities from ground-based radars (with averaging so the vertical air motion is removed) are in the range of $1–2\,m\,s^{-1}$. If we need to reduce the variance below 20% of the magnitude of the observed Doppler velocities, then a horizontal integration of 2500–5000 m is required for the high PRF option and even larger for the low PRF option. If we apply the same requirement to raindrops in large-scale precipitation (with a melting layer and a much higher SNR), then a shorter along-track integration length will be sufficient. Signal integration is a well-established approach for reducing the variance of measurements; however, it comes at the expense of the representativeness of the average value of radar reflectivity and mean Doppler velocity over the integration length. In section 3, the along-track variability of clouds and precipitation in terms of Z variability is examined.

The total error budget of the EC-CPR Doppler velocity measurements includes several other factors such as velocity aliasing, nonuniform beam filling (NUBF), antenna mispointing, and instrument phase error. Particle

sedimentation regimes are characterized by weak vertical motion, and the development of a velocity dealiasing algorithm is straightforward (Ray and Ziegler 1977). Here, the simulated EC-CPR Doppler velocities have been corrected for velocity folding (section 4). However, the development of a velocity-unfolding algorithm in convective areas is expected to be more challenging. A NUBF Doppler velocity correction has been applied to the simulated EC-CPR Doppler velocities (section 4). Another factor that can introduce both bias and increase the uncertainty of Doppler velocity measurements from space is θ_{OP}, the CPR antenna off-nadir pointing. For small angles, the velocity component introduced is proportional to the $V_{sat}\theta_{OP}$ product. It is apparent that in spaceborne Doppler radars, the pointing uncertainty budget needs to be more stringent than those for non-Doppler radars. The correction is straightforward when the mispointing can be characterized by low-frequency harmonics only. Reliable data from the spacecraft navigation system along with referencing antenna-pointing techniques that relay on the earth's surface Doppler velocity measurements (e.g., Testud et al. 1995; Kobayashi and Kumagai 2003; Tanelli et al. 2005) can be used to mitigate this problem. However, small uncertainties in spacecraft attitude can introduce a large Doppler velocity error. For reference to the EC-CPR, an rms of $\theta_{OP} \sim 40\,\mu$rad will introduce an uncertainty of $0.2–0.3\,m\,s^{-1}$. An external calibration method using ground-based active radar calibrators (ARC) has been proposed by JAXA (Horie et al. 2008), and it expected to provide information on the EC-CPR pointing and the quality of the spacecraft navigation data. Errors introduced by antenna mispointing are not included in the analysis of the performance of the EC-CPR Doppler velocity. Furthermore, the impact of the satellite vertical motion is not included in the presented analysis.

b. Synthesis of EC-CPR measurements from ground-based radar data

The generation of synthetic EC-CPR Doppler velocity measurements from the Atmospheric Radiation Measurement Program (ARM) ground-based radar measurements is described in this section. The set of the EC-CPR system configuration parameters is listed in Table 1. A flowchart that indicates the steps in the EC-CPR simulation is shown in Fig. 2. The input scenes can be daily files of 35- and 94-GHz profiling Doppler radar observations (Fig. 3a) from the U.S. Department of Energy (DOE) ARM program facilities (Kollias et al. 2007a; Stokes and Schwartz 1994). The use of the ARM dataset includes some drawbacks: liquid and gaseous attenuation accumulates from the ground-up rather than from top-down as
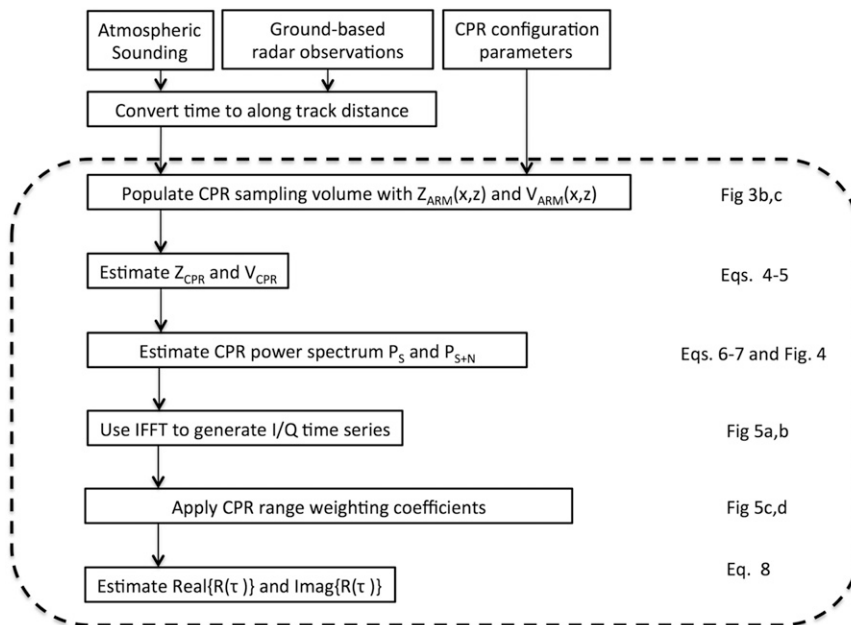
FIG. 2. Flowchart that indicates the various steps of the EC-CPR simulation.

in EC-CPR. This implies that during intense precipitation, the ARM radars observe the highest reflectivities near the ground, whereas the EC-CPR observes them near the top of the liquid layer (Matrosov et al. 2008). However, since this study is concerned with horizontal gradients of radar reflectivity, this should not affect the results if the period with highly variable attenuation is removed. In addition to attenuation, multiple scattering is largely absent in ground-based cloud radar observations, while multiple scattering will frequently occur with the EC-CPR (Battaglia et al. 2011). For these reasons we focused our analysis on scenes not containing deep convection that would have resulted in highly variable and severe attenuation, and multiple scattering effects.

The 94-GHz ARM radar observations are available at 42-m vertical resolution and 4-s integration. An example of ARM radar observations from a midlatitude pre-frontal cirrus cloud observed at the ARM Southern Great Plains site is shown in Fig. 3a. In the EC-CPR simulations, ARM radar time is converted to horizontal distance using the wind profile measurements from the nearest atmospheric sounding at the ARM sites. In a cirrus cloud, the cloud-layer average horizontal wind velocity is used. The impact of the localized (within the CPR sampling volume) horizontal wind shear on the reflectivity structure (e.g., tilted structures) has been already captured in the ground-based observations. Here, for illustration purposes, a $25\,\mathrm{m\,s^{-1}}$ horizontal wind is used. The boxes (Fig. 3a) indicate examples of the EC-CPR sampling volumes, as indicated by its

500-m-range resolution and 700-m footprint. The EC-CPR samples every 100 m in range; thus, there is 5 times oversampling (and significant correlation) in the EC-CPR observations in the vertical column. The horizontal spacing between the centers of the boxes is 1000 m between boxes 1 and 2 and 5000 m between boxes 1 and 3; this provides an indication of the typical horizontal averaging (along-track integration).

Each simulated EC-CPR volume contains $\sim$[7 (horizontal) $\times$ 11 (vertical)] ARM radar observations (NARM = 77), thus providing a good description of the along-track 2D variability within the EC-CPR 700-m footprint (Figs. 3b,c). It is apparent that the resolution of the ARM radar observations is sufficient to describe the conditions within the EC-CPR sampling volume. NUBF (Tanelli et al. 2002a; Schutgens 2008) conditions are observed in all the EC-CPR-simulated sampling volumes, both in the radar reflectivity and the mean Doppler velocity (Figs. 3b,c). Near the cloud edges, the partial beam-filling results in a stretch of the hydrometeor-layer boundaries and the underestimation of the radar reflectivity with respect to the high-resolution ground-based ARM observations.

The expression for the spacecraft-motion-induced Doppler bias can be approximated by expressions dependent only on the along-track distance from nadir x (Tanelli et al. 2002a). The two-way antenna pattern $f^4(\theta, \phi)$ is assumed circularly symmetric and with Gaussian shape. Our simulations are 2D; thus, we are only concerned with the normalized two-way antenna-weighting
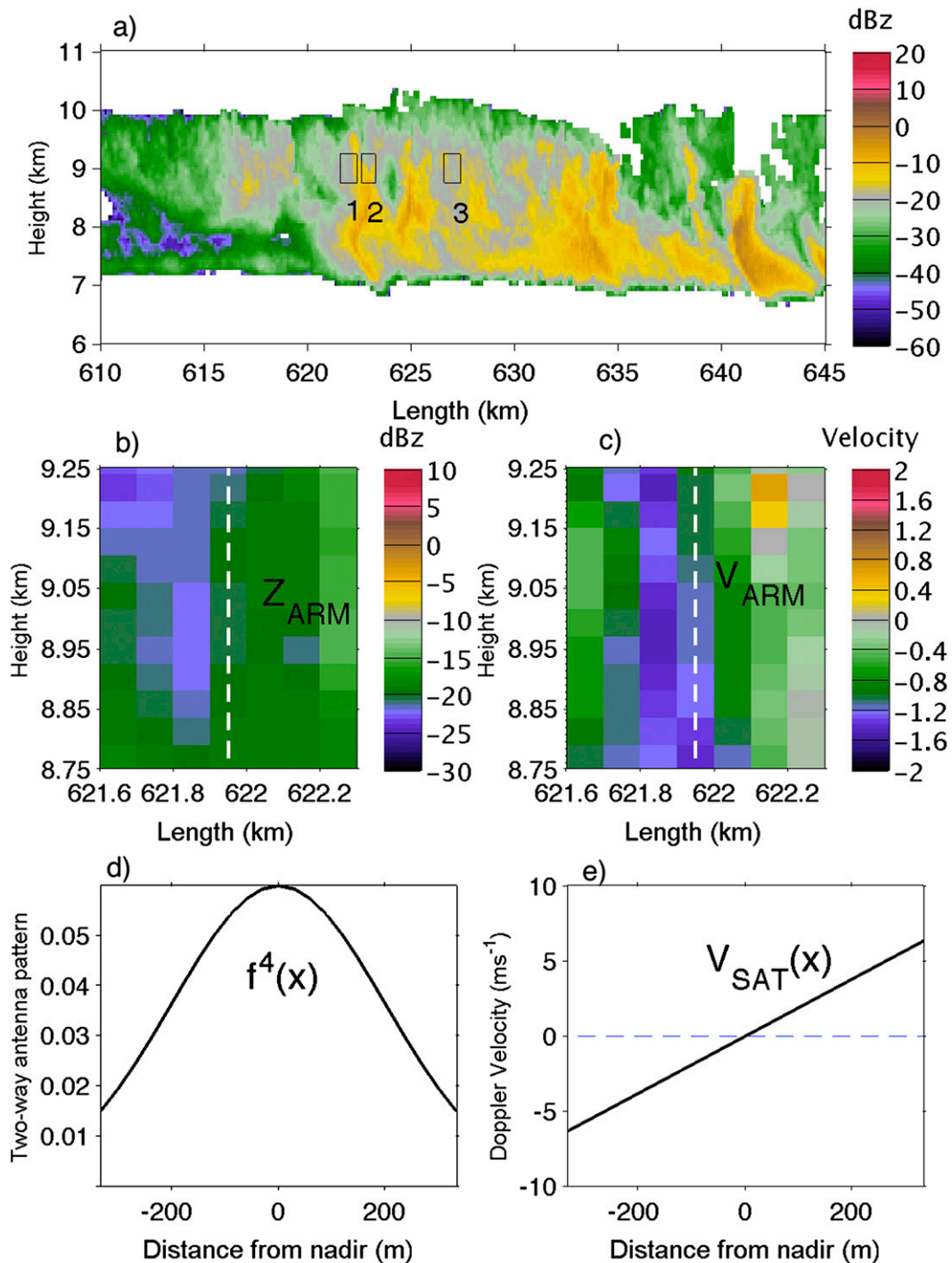
FIG. 3. (a) Example of ARM ground-based radar observations of a midlatitude prefrontal cirrus cloud at the SGP site. The black rectangles (boxes) represent CPR sampling volumes. Volumes 1 and 2 are spaced 1 km apart, and volumes 1 and 3 are spaced 5 km apart. (b),(c) Distribution of ARM radar reflectivity (dBZ) and ARM Doppler velocity (m s^{-1}) within the CPR sampling volume 1, respectively. (d),(e) The antenna-weighting function and the Doppler shift due to the satellite motion as a function of the distance from nadir, respectively.

function $f^4(x)$. This weighting function is applied to all the radar reflectivity ARM $Z_{ARM}(x)$ observations within the sampling volume to estimate the CPR radar reflectivity $Z_{CPR}(x)$ (Fig. 3d):

$$Z_{CPR}(x) = Z_{ARM}(x)f^4(x). \qquad (4)$$

The satellite motion ($V_{sat} \sim 7.6\,\mathrm{km\,s^{-1}}$) is large enough to induce a Doppler shift to the ARM radar volumes within the EC-CPR sampling volume despite its narrow antenna beamwidth. The local Doppler velocity $V_{CPR}(x)$ seen by the EC-CPR is provided by the following approximated expression, valid for small beamwidths and for near-nadir angles (Tanelli et al. 2005):

$$V_{CPR}(x) = \frac{V_{sat}}{H_{sat}}x + V_{ARM}(x), \qquad (5)$$

where the first term represents the Doppler shift induced by the satellite motion and $V_{CPR}(x)$ is the observed ARM radar mean Doppler velocity from the ground. The quantity H_{sat} is the altitude of the CPR. Figure 3e shows the apparent Doppler velocity [first term in Eq. (5)] of the ARM radar volumes due to the motion of the satellite as a function of their distance from nadir.

Centered on each ARM radar data point (along track and height), the simulator defines the EC-CPR sampling volume, and all the ARM observations (Z_{ARM}, V_{ARM}) within the EC-CPR volume are identified (Fig. 4, top). The shaded area (Fig. 4, top) indicates higher radar reflectivity at the forward part of the CPR volume and it induces asymmetry, and thus bias, in the estimated radar Doppler spectrum (Fig. 4, shaded area). The ARM radar observations are converted to their corresponding contributions to the CPR radar reflectivity and velocity [$Z_{CPR}(x)$, $V_{CPR}(x)$] using Eqs. (4) and (5), respectively. The pairs of Z_{CPR} and V_{CPR} are used to construct the ideal (noise free) EC-CPR Doppler spectral density $P_{S,nDFT}$ [n point of the discrete Fourier transform (nDFT); Fig. 4, bottom, black line]. Use of a Doppler spectrum to describe the frequency content of the radar signal requires the use of the stationarity assumption. At a particular range gate, a new EC-CPR Doppler spectrum is estimated every time the satellite moves forward to the next ARM profile, which enters the sampling volume when the last one exits. The time for the EC to move along-track $\Delta L = 100\,\mathrm{m}$ (horizontal spacing between ARM profiles) is equal to $\Delta L/V_{SAT}$, and the number of CPR pulses transmitted within this time interval is $N_p = \mathrm{PRF} \times \Delta L/V_{SAT}$. The synthesized CPR Doppler spectrum is an ideal one (with very large Nyquist velocity $V_{N,CPR}$). This is accomplished by using a very large pulse repetition frequency ($\mathrm{PRF_{IDEAL}}$) that
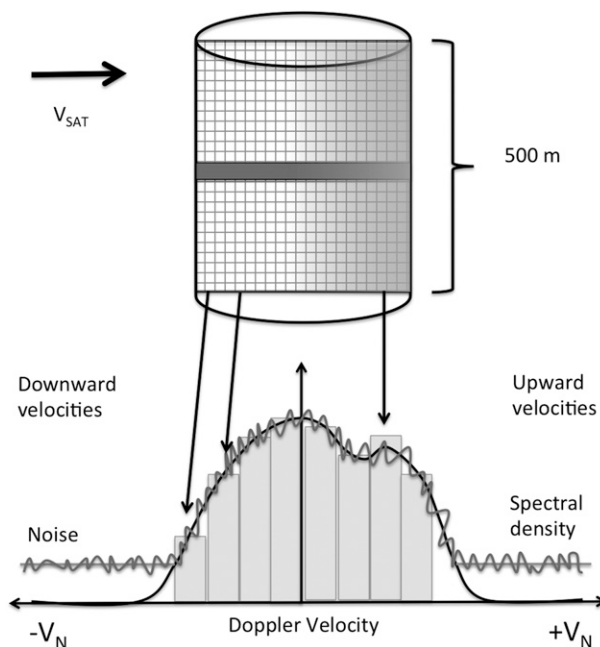

FIG. 4. Example of CPR Doppler spectra construction using the high-resolution ARM radar observations within the CPR sampling volume. (top) The geometry of the CPR simulator with the grid representing the high-resolution ARM observations (not exact match of grid points). The horizontal bar in the middle of the CPR sampling volume represents the ARM gate where the CPR Doppler spectra is constructed using the ARM data above and below. The shading indicates the presence of higher reflectivities in the forward part of the CPR beam. (bottom) The CPR radar Doppler spectra without CPR receiver noise (black line) and with CPR receiver noise (gray line). The vertical bars correspond to velocity displacements of ARM velocities due to motion of the satellite, and the width of the bars indicates the vertical variability of the ARM Doppler velocity at the same displacement off nadir.

is several times (e.g., U times) higher than the actual EC-CPR PRF ($\mathrm{PRF_{IDEAL}} = U \times \mathrm{PRF}$). Thus, the ideal Doppler spectrum Nyquist velocity $V_{N,CPR}$ ($\mathrm{m\,s^{-1}}$) is U times higher than the EC Nyquist velocity ($\pm U \times \mathrm{PRF} \times \lambda/4$) imposed by the selected EC-CPR PRF and wavelength. Furthermore, the number of spectral densities (N_{DFT}) is also U times higher than Np and thus the velocity resolution Δv ($\mathrm{m\,s^{-1}}$) of the EC-CPR Doppler spectrum is preserved. The return atmospheric signal power (average of Z_{CPR} contributions) and the information about the EC-CPR receiver noise power Z_N (total EC-CPR receiver noise is assumed equal to $-21.5\,\mathrm{dB}Z$, estimated using expected CPR sensitivity performance) are used to add noise in the EC-CPR Doppler spectrum (Fig. 4, bottom, gray line). Noise spectrum is assumed white; thus, assuming homogeneous noise contributions, the mean noise spectral density P_N is provided by the following expression:

$$P_N \left(\frac{\text{mm}^6 \, \text{m}^{-3}}{\text{m s}^{-1}} \right) = \frac{Z_N}{N_{\text{DFT}} \Delta v}. \qquad (6)$$

Once the mean noise power density is estimated, a random fluctuation component is added following the method described in Zrnić (1975), so that the spectral power density of the signal-plus-noise $P_{S+N}(i)$ in the ith velocity bin of the spectrum is given by the expression

$$P_{S+N}(i) = -[P_S(i) + P_N] \ln[k(i)], \qquad (7)$$

where k is a random number uniformly distributed between 0 and 1 (Fig. 4, bottom, eight gray lines).

The CPR sampling volume is shifted vertically at each ARM range gate, and this process generates a vertical stack of CPR Doppler spectra (Fig. 5a). The next step is to apply inverse discrete Fourier transform (IDFT) of the constructed CPR Doppler spectrum in order to retrieve in-phase (I) and quadrature-phase (Q) voltage time series (Zrnić 1975). The generated I/Q radar time series at each ARM range gate are subsequently undersampled by a factor U to simulate the actual PRF of the EC-CPR. Examples of I time series generated by the IDFT operation are shown in Fig. 5b. The amplitude of the I time series corresponds well with the intensity of the CPR Doppler spectral densities. The I time series also appear vertically uncorrelated. However, because of the EC-CPR range-weighting function $W(r)$, the I/Q samples of the CPR at consecutive range gates (spaced by 100 m) should be correlated (Fig. 5c). Thus, the I (and Q) samples corresponding to the same EC-CPR pulse are convoluted with $W(r)$. The outcome is I/Q time series correlated with height (Fig. 5d) according to the EC-CPR range resolution and spaced at the EC-CPR range sampling.

The described process generates Np I/Q radar samples every ΔL along-track displacement of the satellite. In the next step, the simulator moves ΔL to the next ARM radar data profile and generates another set of Np I/Q radar samples. After integrating over 500 m (EC-CPR along-track integration distance), the generated I/Q radar samples have length $M = N_p(500/\Delta L)$ and are used to estimate (Kobayashi et al. 2002) the first three radar Doppler moments (radar reflectivity, mean Doppler velocity, Doppler spectrum width) using the autocovariance analysis by means of the PP processing technique (Zrnić 1977). In the time domain, the radar complex signal $C(t) = I(t) + jQ(t)$ is used to calculate the autocovariance $R(\tau)$ at lag one—for example, from pulse to pulse:

$$\hat{R}(\tau) = \frac{1}{M-1} \sum_{i=1}^{M-1} C^*(i) C(i+1) \qquad (8)$$

$$\hat{v} = \frac{\lambda \times \text{PRF}}{4\pi} \arctan \left\{ \frac{\text{Im}[\hat{R}(\tau)]}{\text{Re}[\hat{R}(\tau)]} \right\} \qquad (9)$$

The real and imaginary parts of the autocovariance $\hat{R}(\tau)$ [Eq. (8)] are then used to estimate the mean Doppler velocity $\hat{v}$ [Eq. (9)]. In case of longer integration length (e.g., 1000–5000 m), the raw real and imaginary parts of $\hat{R}(\tau)$ are first corrected for NUBF and, subsequently, their mean average values are used to estimate the Doppler velocity of the echo.

3. Climatology of Z variability in clouds and precipitation

To assess the impact of (500–5000 m) along-track integration of CPR measurements, a large dataset of ARM ground-based 94-GHz radar measurements is used. The dataset comes from four separate deployments (see Table 2) of the W-band ARM Program Cloud Radar (WACR) system (Widener and Mead 2004). The ARM Mobile Facility (AMF) deployment at Niamey, Niger (NIM, 8 months of observations, 2006); the AMF deployment at the Black Forest, Germany (FKB, 8 months of observations, 2007); the AMF deployment at Graciosa Island, Azores (GRW, 19 months of observations (2009–10); and the deployment of the WACR at the ARM Southern Great Plains (SGP, 2 months, 2006). During the NIM deployment, the typical cloud conditions were cirrus clouds and extensive precipitation systems; during the FKB deployment, low-level clouds and extensive orographic precipitation with low melting layer; during the GRW deployment, extensive marine stratocumulus conditions, broken cumulus, and frontal systems; and during the SGP deployment, frontal precipitating systems.

The WACR data have 4-s temporal resolution and 42-m vertical resolution, and cover from 150 m above the ground to 15-km height. At each WACR range gate, the radar reflectivity difference (ΔZ) for fixed horizontal lengths (500, 1000, 2500, and 5000 m) is recorded using observations spaced by the aforementioned horizontal lengths. At cloud edges, ΔZ is not defined and thus the analysis does not include gradients near cloud boundaries. For each selected horizontal length, the average radar reflectivity $\langle Z \rangle$ is estimated using all the available WACR reflectivity values within the horizontal length, and temperature T from the nearest sounding interpolation is also recorded. Furthermore, a +5-dBZ radar reflectivity threshold at 300 m above the ground is used to separate the WACR profiles into precipitating and nonprecipitating groups.

The selection of the horizontal lengths used in the climatology is determined by the EC-CPR parameters.
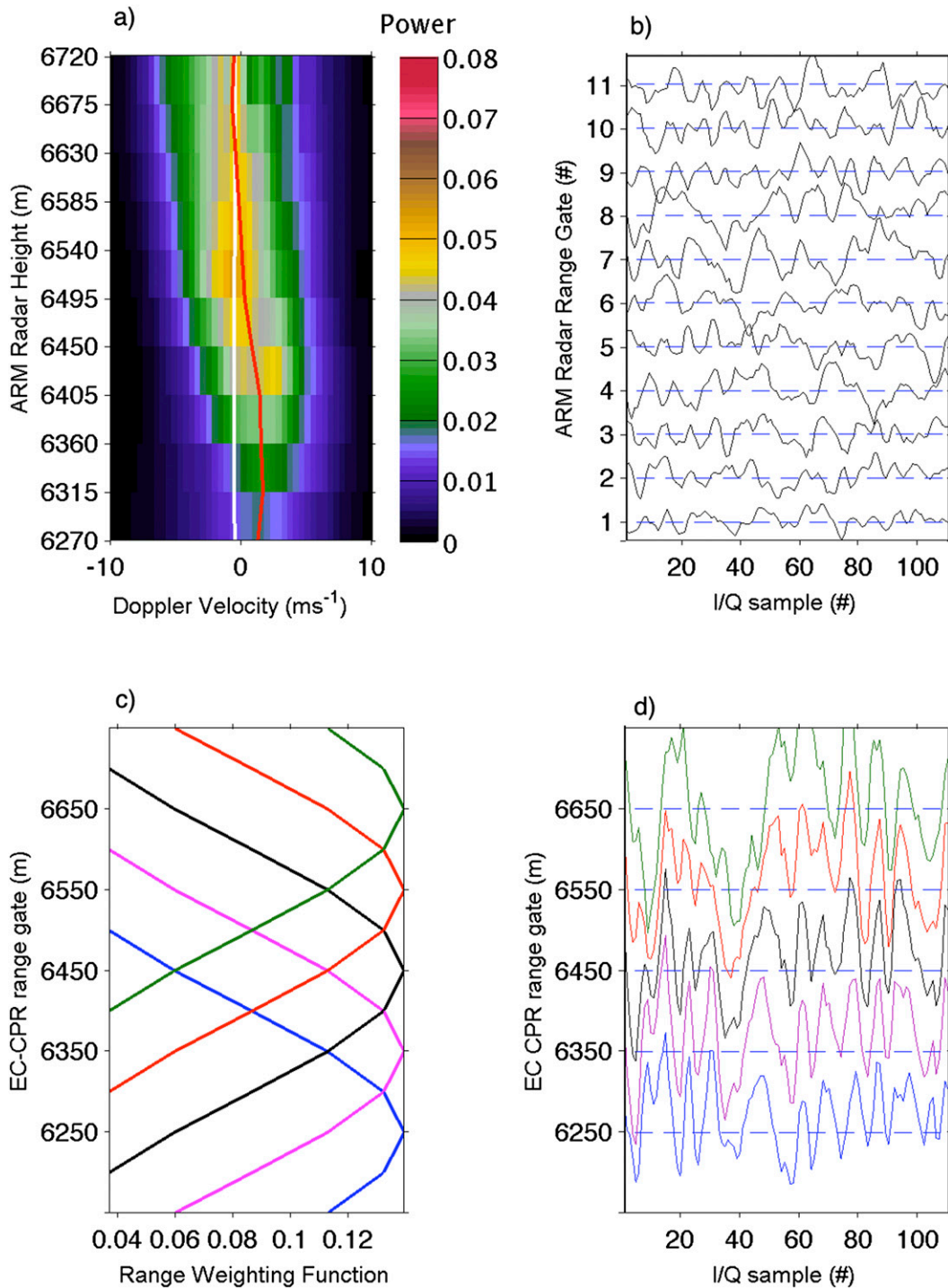
FIG. 5. (a) Vertical stack of simulated CPR Doppler spectra at different ARM range gates. The red line is the NUBF Doppler bias estimated by the distribution of ARM radar observations within the CPR sampling volume. (b) ARM I/Q radar time series generated from the inverse fast Fourier transform. There is one I/Q time series for each spectrogram displayed in (a). There are 110 samples of I or Q in each height collected in 15.7 ms of along-track integration (PRF = 7 kHz). (c) The radar range-weighting function repeated every 100 m. (d) The I/Q CPR radar time series after the along-range convolution of the ARM I/Q radar time series with the CPR range-weighting function. Notice the vertical correlation between the I/Q time series.

TABLE 1. EarthCARE CPR technical characteristics.

Frequency (GHz)	94.05
PRF (kHz)	6.1–7.5
Antenna diameter (m)	2.5
Beamwidth (°)	0.095
Altitude (km)	400
Beam footprint (m)	700
Vertical resolution (m)	500 (3.3-μs pulse)
Vertical sampling (m)	100
Along-track integration (m)	500
Sensitivity (dBZ)	−21.5 (single pulse)
	−35 (10-km integration)

The minimum along-track integration length of the CPR is 500 m; thus, no CPR observable will be available in higher resolution. The estimation of ΔZ from the EC-CPR reflectivity measurements requires a minimum of two measurements; thus, ΔZ measurements will be available every 1000 m. The ΔZ measurements every 1000 m (ΔZ_{1000}, dB km^{-1}) will be used to assess the NUBF velocity bias VNUBF in the CPR Doppler velocities (Tanelli et al. 2002a). Finally, the 2500- and 5000-m horizontal lengths are used here to provide information on the cloud and precipitation inhomogeneity over longer integration lengths.

The cumulative distribution functions of ΔZ for the four horizontal lengths and for the WACR deployments are shown in Fig. 6. The results are similar in all four sites. At 1000-m length, 63%, 67%, 66%, and 68% of the measured ΔZ_{1000} are below 3 dB km^{-1} at the FKG, GRW, NIA, and SGP sites, respectively. This is the horizontal length where the NUBF Doppler velocity corrections will be applied. The fraction of ΔZ changes that are less than 3 dB decreases significantly with horizontal distance in clouds and precipitation. At 5000-m length, 46%, 50%, 49%, and 52% of the measured ΔZ_{5000} are below 3 dB km^{-1} at the FKG, GRW, NIA, and SGP sites, respectively. The observed, along-track inhomogeneity of the radar reflectivity affects the integration length of the EC-CPR Doppler velocity measurements in two ways: First, every 500 m, a NUBF Doppler velocity bias correction needs to be applied (see section 4). However, the NUBF correction is based on the assumption that two EC-CPR reflectivity measurements spaced 1000 m apart are sufficient to describe the NUBF conditions (i.e., the along-track radar reflectivity field varies linearly). Any departure from this assumption will result to accumulating NUBF Doppler velocities biases within the integration length. Second, even if the NUBF correction is applied correctly, the question of representativeness of EC-CPR Doppler velocities over an along-track length that is characterized by significant radar reflectivity is open. In section 4c, this issue is revisited.

These issues are amplified in the case of marine stratus clouds, which are of particular interest to the EC scientific community due to their important impact on the boundary layer dynamics and global climate (Bony and Dufresne 2005). In particular, the representation of drizzle in numerical models is a challenge of current concern, especially since drizzle is ubiquitous in marine stratocumulus (e.g., Serpetzoglou et al. 2008). This cloud type is a challenging target for the EC-CPR (as it has been for *CloudSat*; Tanelli et al. 2008) due to the expected contamination of the lowest 0.75–1.2 km by the surface echo. The EC-CPR features higher along-range sampling (100 m) that could be useful in characterizing the CPR echo structure near the surface (lowest 1.2 km). This can assist in subtracting an estimate of the surface clutter from the total measured return power near the surface and thus improve the detection of clouds close to the earth's surface. However, the main factor determining the vertical extent of the surface echo is the pulse length. The EC-CPR uses the same pulse length as *CloudSat*, and the details of the EC-CPR receiver point-target-response function (not available at this point) will determine any improvement that the EC-CPR will have over *CloudSat* in detecting low-level clouds. Nevertheless, using the large dataset from the AMF deployment at GRW, a targeted (limited to the lowest 2 km and for high-cloud-fraction conditions) analysis of the horizontal variability of marine stratiform clouds is shown in Fig. 7. The analysis indicates that these "allegedly" homogeneous stratiform clouds have large Z variability that exceeds the climatological values derived at the four ARM sites (Fig. 6). At 1000 m, 56% of the measured ΔZ_{1000} are below 3 dB km^{-1} and at 5000 m, the percent drops to 47%. The presence of large horizontal

TABLE 2. ARM sites and data periods used in the climatology.

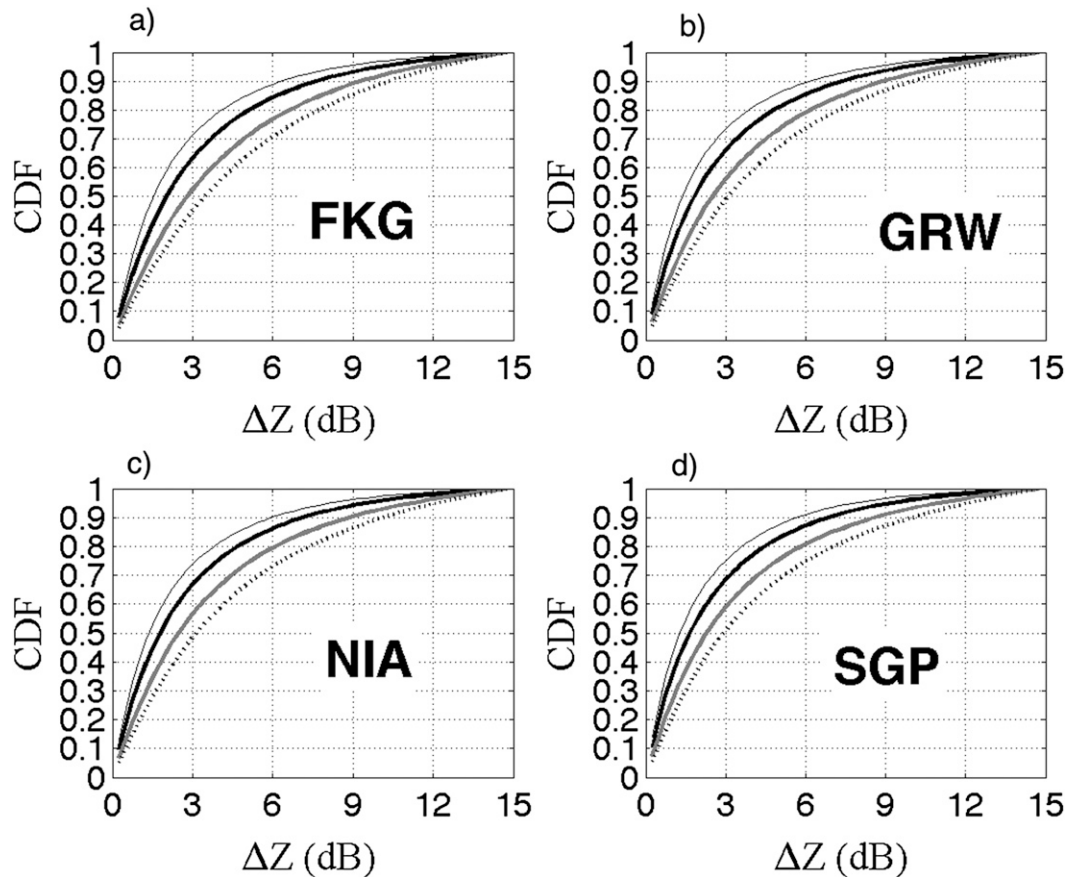| Site	Latitude	Longitude	Record (months)	Start	End
FKB	48°32′24.18″N	8°23′48.7″E	8	1 Apr 2006	31 Dec 2006
GRW	39°5′ 28″N	28°1′ 45″W	19	1 May 2009	30 Nov 2010
NIM	13°28′39.15″N	2°10′27.62″E	8	1 Apr 2007	31 Dec 2007
SGP	36°36′18.0″N	97°29′6.0″W	2	1 May 2007	1 Jul 2007

FIG. 6. Cumulative distribution functions of observed ΔZ changes at (a) FKB, (b) GRW, (c) NIA, and (d) SGP for four different horizontal lengths: 500 (thin gray), 100 (thick black), 2500 (thick gray), and 5000 m (dotted gray).

variability, combined with the shallow nature of these stratiform clouds and their low reflectivity values make the use of the CPR Doppler velocity challenging.

4. Synthetic EC-CPR observations

The described EC-CPR simulator (section 2) is applied to 40 different cloud scenes (20 cirrus clouds and 20 large-scale precipitation cases) observed by the WACR at the ARM fixed and mobile sites (SGP, FKB, NIM, and GRW). Each case consists of 6–15 h of observations, with an average thickness of 4 km for the cirrus layers and an average thickness of 10 km for the precipitation systems. Considering that the WACR vertical resolution is 45 m and its temporal resolution is 4 s, the total simulated WACR dataset included more than 60 million data points.

The presented EC-CPR-simulated Doppler velocities have been corrected for NUBF and aliasing. In general, V_{NUBF} can be expresses as a function of the distribution of the radar reflectivity field in the along-track direction within the EC-CPR sampling volume (Tanelli et al.

2002a). This information however, is not available in EC-CPR measurements. The only information available to characterize the along-track variability of the radar reflectivity is the gradient of radar reflectivity ΔZ_{1000} from the EC-CPR. In this case, V_{NUBF} can be expressed as

$$V_{\mathrm{NUBF}} = \alpha \Delta Z_{1000}, \qquad (10)$$

where α [m s^{-1} (dB km^{-1})$^{-1}$] is a constant that depends on the along-track weighting function $f^4(x)$ of the CPR and the along-track variability of the radar reflectivity with the CPR volume. Here, a mean value for the parameter α is estimated using the CPR simulation framework and all simulated WACR cases. For each EC-CPR sampling volume (see Fig. 4b), the velocity bias induced due to NUBF (VNUBF) is estimated by replacing all ARM radar velocities (see Fig. 4d) with zero. In this case, only the inhomogeneous distribution of ARM radar reflectivities within the EC-CPR volume contributes to the simulated Doppler velocity. The along-track gradient of the radar reflectivity (ΔZ_{1000}) is estimated by the EC-CPR simulated radar reflectivities.
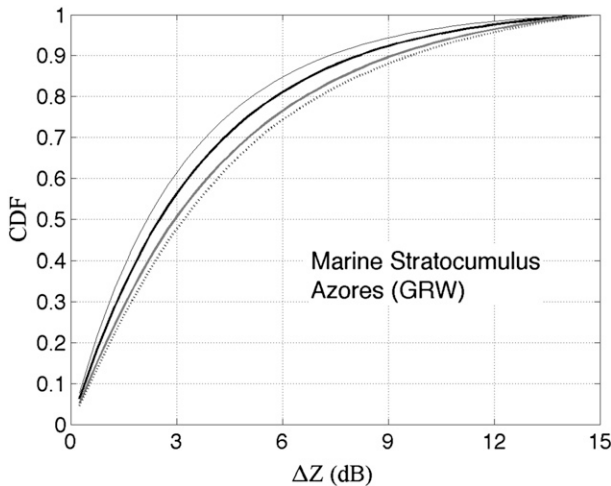
FIG. 7. Cumulative probability distributions function of observed ΔZ for different horizontal lengths: 500 (thin gray), 1000 (thick black), 2500 (thick gray), and 5000 m (dotted gray) in marine stratocumulus observed by the WACR during the AMF GRW deployment. Only WACR cloud detections in the lowest 2 km of the atmosphere and with high-cloud-fraction conditions (above 80%) have been used.

Using all available (V_{NUBF}, ΔZ_{1000}) pairs in a particular height in a cirrus or a precipitation system, the parameter α [m s^{-1} (dB km^{-1})$^{-1}$] is estimated using linear regression fit (Fig. 8a). The distribution of all α values estimated using the entire simulated WACR dataset is shown in Fig. 8b. The mean value of α is 0.2297 m s^{-1} (dB km^{-1})$^{-1}$ and its standard deviation is 0.0167 m s^{-1} (dB km^{-1})$^{-1}$. Thus, a ΔZ_{1000} of 3 dB (doubling of Z) will produce a CPR Doppler velocity bias of 0.69 m s^{-1}; a ΔZ_{1000} of 6 dB is available as output of the EC-CPR simulators, and the entire dataset is corrected using the estimated mean value of the parameter α [m s^{-1} (dB km^{-1})$^{-1}$].

In addition to the NUBF correction, the simulated EC-CPR Doppler velocities are also corrected for velocity folding. For the selected cloud systems, the vertical air motion is expected to be weak, $|w_{\text{air}}| < 2$ m s^{-1}. This assumption greatly simplifies the velocity-unfolding algorithm that assumes that aliasing can occur only due to the large sedimentation velocity of large hydrometeors. The velocity unfolding is a two-step process. First, if the simulated EC-CPR Doppler velocity is higher than $+3$ m s^{-1} (updraft) and the EC-CPR-simulated reflectivity is higher than -5 dBZ, then the EC-CPR Doppler velocity is unfolded using the following expression:

$$V_{\text{unfolded}} = V_{\text{Folded}} - 2V_N. \tag{11}$$

Following this step, the along-track EC-CPR Doppler velocity gradient is estimated, and its value is used to

identify the remaining folded velocities that are also unfolded using Eq. (11).

Here are two representative cloud cases sampled by the ARM 94-GHz radars in an attempt to illustrate key features of the expected performance of the EC-CPR in particle sedimentation areas. The first cloud system is a long-lived thick cirrus cloud observed at the SGP, and the second is an extensive stratiform precipitation case observed at the NIM deployment.

a. Cirrus cloud case

The ARM WACR ground-based observations of the extensive cirrus cloud are shown in Fig. 9. The hydrometeor-layer average horizontal wind speed is used to convert time to horizontal length in the WACR data. The cirrus-layer thickness varied from 3.5 km at the beginning of the period to 5.0 km at the end of cirrus hydrometeor cluster (Fig. 9a). On average, the radar reflectivity increases toward the cirrus cloud base, indicating particle growth. The estimated V_{NUBF} every 500 m of signal integration is shown in Fig. 9b. As discussed previously, the V_{NUBF} is estimated by replacing the ARM radar Doppler velocity field with zero. The V_{NUBF} field structure resembles the WACR radar reflectivity field (Fig. 9a) with tilted structures similar to the fall streaks. The largest NUBF Doppler velocity biases are observed near the cloud boundaries. This is consistent with the partial beam filling of the CPR sampling volume (hydrometeor filled vs hydrometeor free volumes). Away from cloud boundaries, the NUBF Doppler velocity biases are relatively small (± 0.5 m s^{-1}).

The WACR Doppler velocity field is shown in Fig. 10a. The increased downward Doppler velocities in the lower part of the cirrus cloud are consistent with the presence of higher reflectivities near the base of the cirrus layer. Near the cirrus layer, mammatus clouds are shown in the velocity and reflectivity images. The black contour indicates the area of the cirrus cloud with radar reflectivity above -21.5 dBZ and thus above zero SNR conditions for EC-CPR. The simulated CPR Doppler velocities every 100 m range and with a horizontal integration of 1000 m [nominal CPR level 2 a (L2a) Doppler velocity product resolution] are shown in Fig. 10b. The simulated CPR Doppler velocities have been corrected for NUBF biases [Eq. (10)] using the simulated CPR radar reflectivities to estimate ΔZ_{1000} and using the mean value of α [m s^{-1} (dB km^{-1})$^{-1}$]. As expected, near the cloud edges and in areas with low radar reflectivities, the CPR-simulated velocity field is noisy. Within the cirrus area with higher WACR reflectivities, the simulated CPR Doppler velocities are more in agreement with the input WACR Doppler velocities (Fig. 10b); however, large uncertainty is observed. The simulated CPR Doppler velocities every
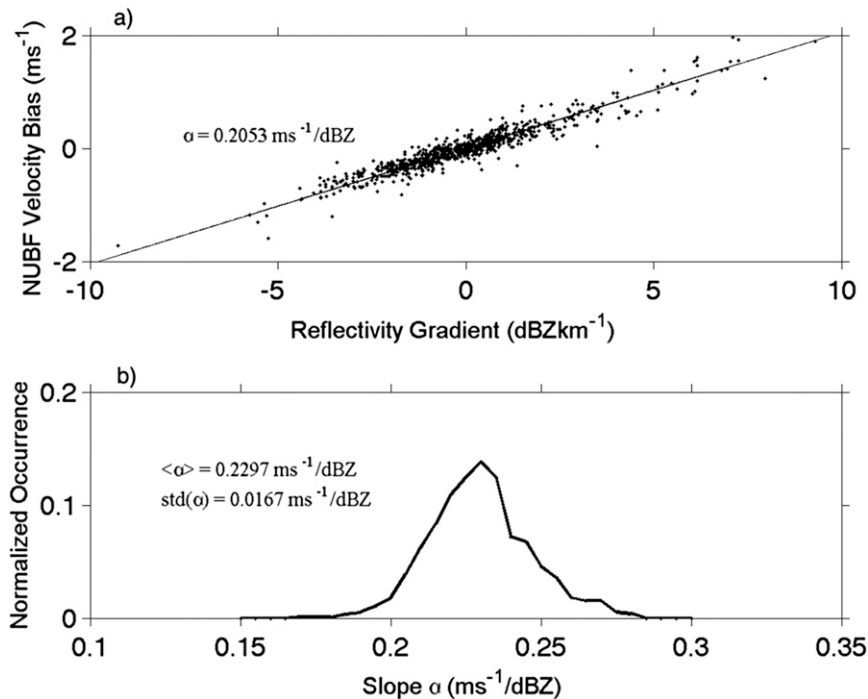
FIG. 8. (a) Example estimation of the parameter α using simulated EC-CPR data at a particular height. The parameter is estimated as the slope of the linear regression fit. (b) The distribution of all α values estimated using all simulated WACR cloud and precipitation cases. At each EC-CPR range gate and for each simulated cloud and precipitation system, an α value is estimated using all available simulations at this range gate.

100 m range and with a 5000-m horizontal integration are shown in Fig. 10c. Longer CPR signal integration has no effect on the CPR Doppler estimates at very low SNR conditions. However, the simulated CPR Doppler velocity estimates within the area of high SNR is smoother and resembles the original WACR Doppler velocity measurements.

b. Large-scale precipitation case

The ARM WACR ground-based observations of the extensive large-scale precipitation period from NIM are shown in Fig. 11. The extensive precipitating system persisted for over 700 km (over 20 h, with an average horizontal wind of $10 \, \mathrm{m \, s^{-1}}$) with an initial short-lived convective period (centered on 200-km-length location) that attenuated significantly the WACR signal and effectively reduced the detected cloud top from 13 km to as low as 5 km. Understandably, the bottom-up view of precipitation from the WACR is very different from the top-down view from a spaceborne radar; however, our analysis focuses on the trailing stratiform part of the studied precipitating system. The melting layer is at 4.2 km and can be observed by the WACR radar reflectivity jump (Kollias and Albrecht 2005). The black contour indicates the area of precipitation with SNR > 0.

The simulated NUBF CPR Doppler velocity biases every 500 m of the signal integration are shown in Fig. 11b. As it was the case in the cirrus cloud simulation, the largest NUBF Doppler velocity biases are observed near the cloud and precipitation boundaries. Away from cloud boundaries, the NUBF Doppler velocity biases are relatively small ($\pm 0.5 \, \mathrm{m \, s^{-1}}$).

The WACR Doppler velocity field is shown in Fig. 12a. The WACR Nyquist velocity is $8 \, \mathrm{m \, s^{-1}}$, and it is sufficiently large to avoid velocity folding in this case. The transition from the ice phase to the liquid phase is clearly delineated at 5 km in height by the WACR Doppler velocity field. The simulated CPR Doppler velocities for every 100-m range and with a horizontal integration of 1000 m are shown in Fig. 12b. In this case, the areas with low WACR reflectivities are only a small fraction of the observed system; although, due to attenuation, it is possible that the WACR does not detect a significant part of the upper part of the cloud. Although there are large uncertainties, the simulated CPR Doppler velocities clearly capture the signature of the melting layer in the precipitation. There are several areas, especially early in the convective period, where the simulated CPR Doppler velocities are positive (upward). This is attributed to velocity folding and occurs
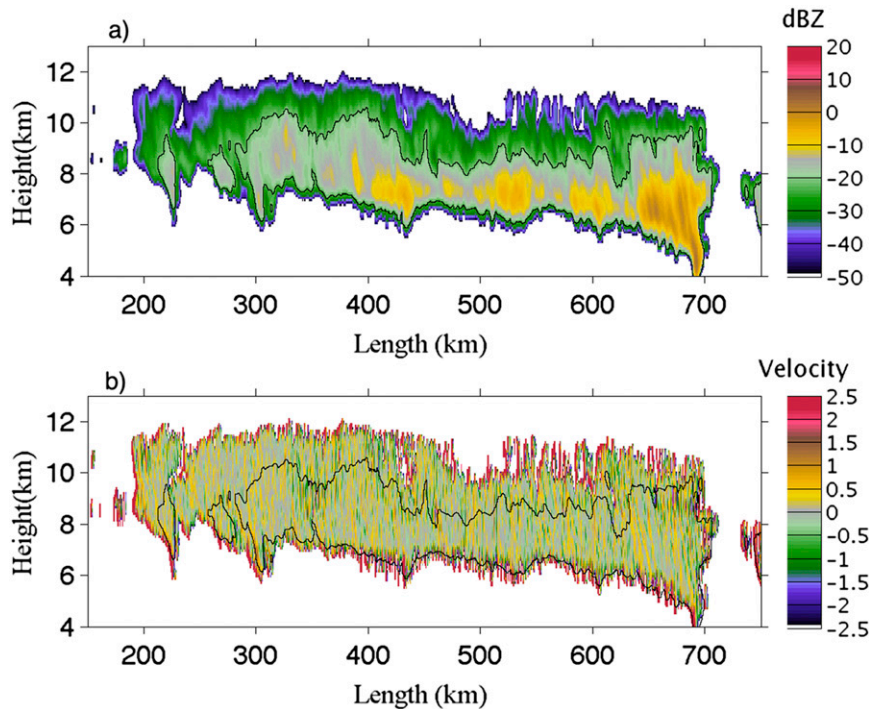
FIG. 9. Horizontal length vs height plots of (a) the WACR radar reflectivity and (b) estimated NUBF Doppler velocity bias $(m\,s^{-1})$. The black contour indicates the cirrus area with radar reflectivity above $-21.5\,dBZ$.

when the combination of reflectivity-weighted hydrometeor fall velocity and the vertical updraft–downdraft motions exceed the EC-CPR Nyquist velocity V_N. Thus, even in ideal conditions (uniform beam filling and no antenna mispointing), EC-CPR Doppler measurements in precipitation will suffer from velocity aliasing that needs to be corrected, as is done in ground-based and airborne Doppler radars. The simulated CPR Doppler velocities for every 100 m with a 5000-m horizontal integration are shown in Fig. 12c. The simulated CPR Doppler velocity estimates within the area of high SNR is smoother and resembles the original WACR Doppler velocity measurements.

c. Comparison of WACR and simulated CPR Doppler measurements

A comparison between observed ARM radar Doppler velocity measurements and simulated CPR Doppler velocity estimates is provided in Fig. 13. Four different cloud systems have been simulated: a cirrus case observed on 22 November 2004 at the SGP (Fig. 13a), a cirrus case observed on 7 March 2006 at Darwin (Fig. 13b), a stratiform precipitation case observed on 28 August 2006 at NIM, (Fig. 13c), and a stratiform precipitation case observed on 1 June 2007 at FKB (Fig. 13d). On average, 10 h of ground-based observations

have been used in each case to estimate the profiles of the mean Doppler velocity and its standard deviation. The ARM radar Doppler observations have been averaged over 5000 m at each height, and the simulated EC-CPR Doppler velocities are generated using 5000 m of along-track integration. At each height, the mean and the standard deviation of observed (ARM) Doppler velocities are shown in black and the mean and standard deviation of the simulated (CPR) Doppler velocities are shown in red. Only Doppler velocities that correspond to radar reflectivities above $-15\,dBZ$ are used in the calculation of the statistics shown in Fig. 13. Overall, there is agreement between the observed and simulated mean profiles. In the cirrus cases, the differences are higher near the cloud edges. This is consistent with the presence of more variable conditions near the cloud boundaries that can produce complicated NUBF conditions that cannot be corrected using the linear gradient approximation [Eq. (10)]. In the precipitation cases, the larger differences are observed in the deep liquid precipitation layer in NIM (Fig. 13c), consistent with the presence of large variability due to subcloud layer evaporation. The simulated EC CPR Doppler velocities have a higher standard deviation.

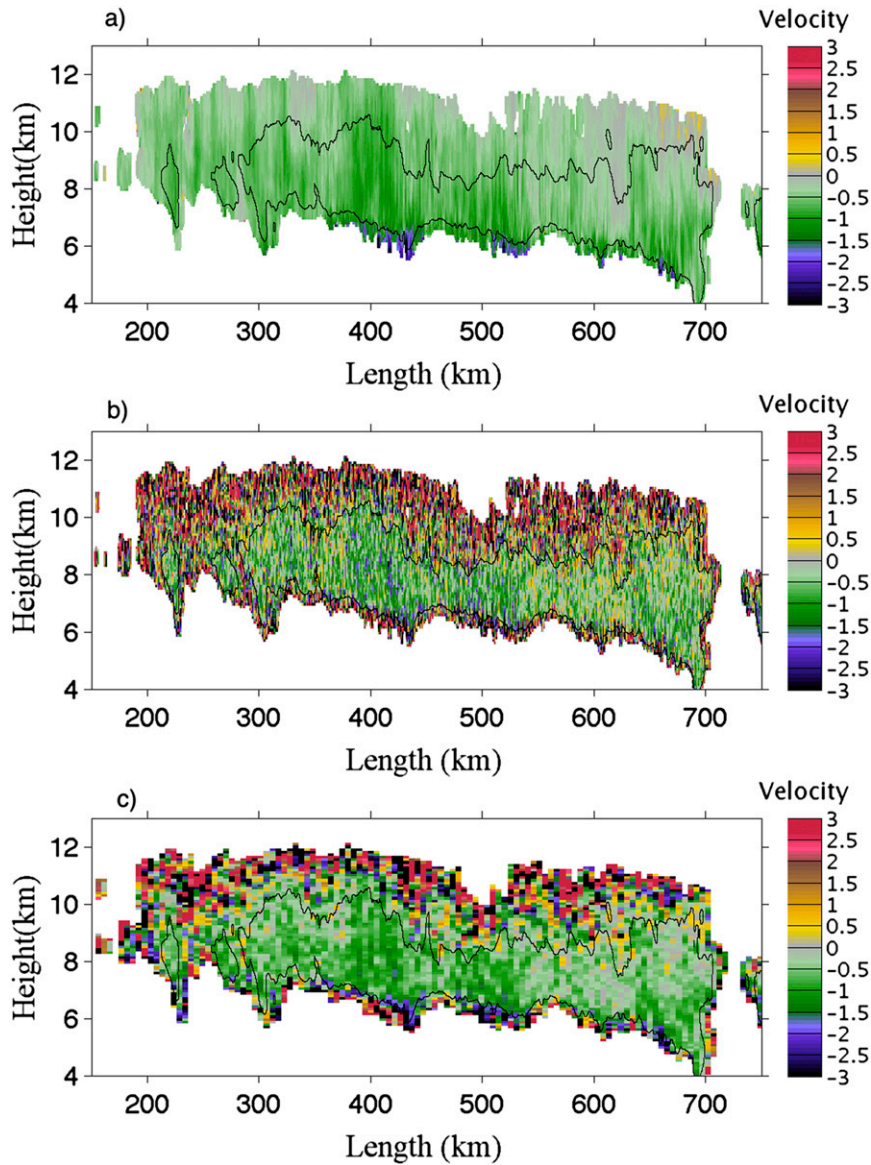Finally, using all simulated cases (20 cirrus and 20 precipitation cases observed by the ARM WACR), the

FIG. 10. Horizontal length vs height plots of (a) the WACR mean Doppler velocity (m s^{-1}) and (b),(c) the simulated CPR Doppler velocity estimates for a 1000- and 500-m signal integration, respectively The EC-CPR PRF is 7000 Hz.

uncertainty in the EC-CPR Doppler velocity measurements is estimated. The results are classified to cirrus clouds and stratiform precipitation systems, and are available for two different CPR along-track integration lengths (1000 and 5000 m). At each EC-CPR range gate, the root-mean-square deviation (RMSD) between the observed and simulated Doppler velocities is estimated using the following expression:

$$\text{RMSD} = \sqrt{\frac{\sum_{i=1}^{n} [V_{\text{ARM}}(i) - V_{\text{CPR}}(i)]^2}{n}} . \quad (12)$$

Only EC-CPR-simulated Doppler velocities with a radar reflectivity higher than -15 are used in the RMSD estimation. The RMSD estimates from each CPR range gate and for all simulated cloud and precipitation systems are used to produce the RMSD histograms shown in Fig. 14. The total number of data points $(V_{\text{ARM}}, V_{\text{CPR}})$ used for each histogram is 169 000 (Fig. 14a), 33 790 (Fig. 14b), 616 000 (Fig. 14c), and 123 300 (Fig. 14d). In addition to the aforementioned classifications (cirrus vs stratiform precipitation) and (1000 vs 5000 m), the RMSD statistics are displayed with and without the NUBF Doppler velocity bias correction applied. In all
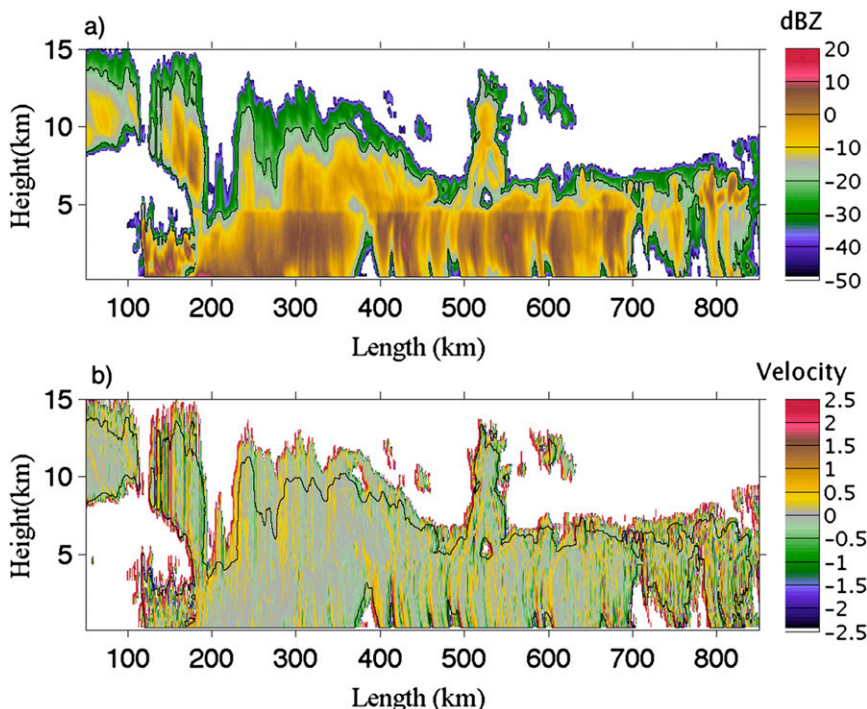
FIG. 11. Horizontal length vs height plots of (a) the WACR radar reflectivity and (b) estimated NUBF Doppler velocity bias. The black contour indicates the precipitation area with radar reflectivity above −21.5 dBZ.

cases, the implementation of the NUBF Doppler velocity bias correction improves the comparison (shifting of the histograms to lower RMSD values) between the WACR and the CPR-simulated Doppler velocities. The NUBF Doppler velocity correction impacts more the quality of the CPR Doppler velocities in terms of RMSD values at 1-km integration (0.12–0.15 m s^{-1} improvement in the mean RMSD) compared to a 0.02–0.03 m s^{-1} improvement at 5-km integration. This can be attributed to the canceling of NUBF velocity biases as the integration length increases. Most of the improvement in the NUBF-corrected mean RMSD values from 1- to 5-km integration for both cirrus (0.44 from 0.84 m s^{-1}) and precipitation (0.27 from 0.54 m s^{-1}) cases can be attributed to the factor of increase in the number of CPR I/Q samples used in the estimation of the CPR Doppler velocities. Finally, the lower RMSD values in precipitation are attributed to the higher SNR conditions encountered in precipitation.

5. Summary

An EC-CPR Doppler velocity simulator is developed to provide an assessment of the quality of the EC-CPR Doppler measurements in nonconvective regimes. Excluding factors related to the CPR hardware (e.g., transmitter phase noise), the quality of the EC-CPR

Doppler velocity measurements is affected by three main factors due to the spacecraft motion:

- Doppler broadening constant along a profile in presence of homogeneous fields of reflectivity: this broadening contributes to the total spectral width in rms sense, and "whitens" the Doppler spectrum, and therefore reduces the Doppler accuracy.
- Doppler bias, variable along the profile, in presence of nonhomogeneities inside each volume of resolution: the bias term is proportional to the along-track gradient of measured backscattered power within the volume of resolution.
- Doppler bias constant along a radar profile introduced by antenna mispointing: this bias can amount to several meters per second, and only a portion of it can be removed using the a priori knowledge of the pointing and navigation coordinates of the radar.

The uncertainty in EC-CPR Doppler measurements introduced by the antenna mispointing is not discussed in the total error budget here. Furthermore, the selected cloud and precipitation systems are characterized by weak vertical motion and small radar reflectivity gradients. Thus, the presented analysis should be considered as the best-case scenario. Three different methods are used to assess the impact of the first two factors on the
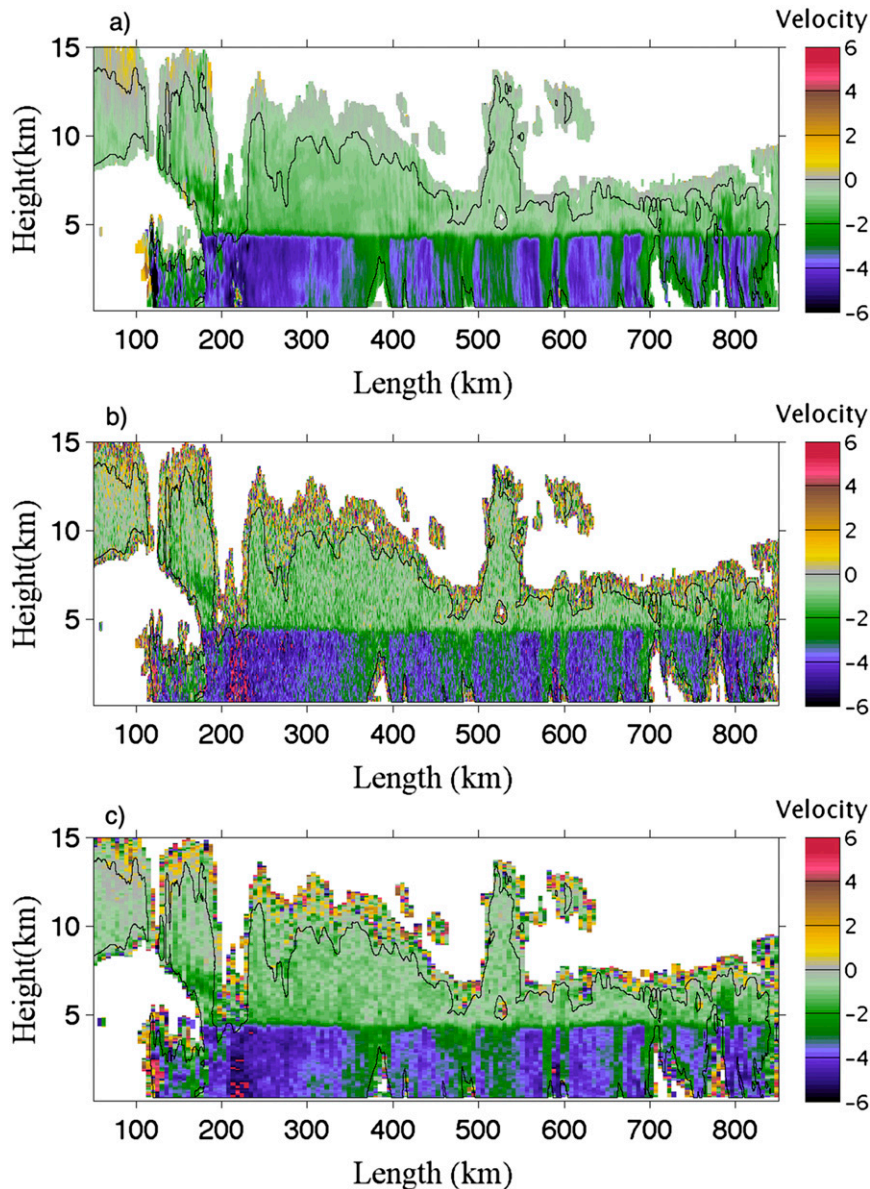
FIG. 12. Horizontal length vs height plots of (a) the WACR mean Doppler velocity and (b),(c) the simulated CPR Doppler velocity estimates for a 1000- and 5000-m signal integration, respectively, The EC-CPR PRF is 7000 Hz.

CPR Doppler performance. First, CPR raw signal simulations for uniform beam-filling conditions were performed using the CPR operational parameters to assess the impact of the Doppler broadening factor (section 2a). Similar simulations have been carried out in the past for more generic spaceborne radar concepts (e.g., Tanelli et al. 2002a,b). Here, the analysis focuses on the EC-CPR and indicates that the CPR Doppler velocity measurements at low SNR conditions (below $-21.5 \, dBZ$) will have large uncertainties and will be challenging to use for scientific applications. The analysis indicates

that signal integration (2500–5000 m) is needed to reduce the Doppler velocity standard deviation below $0.5 \, m \, s^{-1}$. The suggestion of along-track integration to reduce the uncertainty in CPR Doppler measurements is not new, and there is no penalty if the cloud and/or precipitation scenes are homogeneous for the duration of the integration. It is important to highlight the impact of the PRF on the Doppler velocity uncertainty in uniform conditions. The EC-CPR is expected to have much better Doppler performance at high latitudes (above 60°) compared to the tropics and
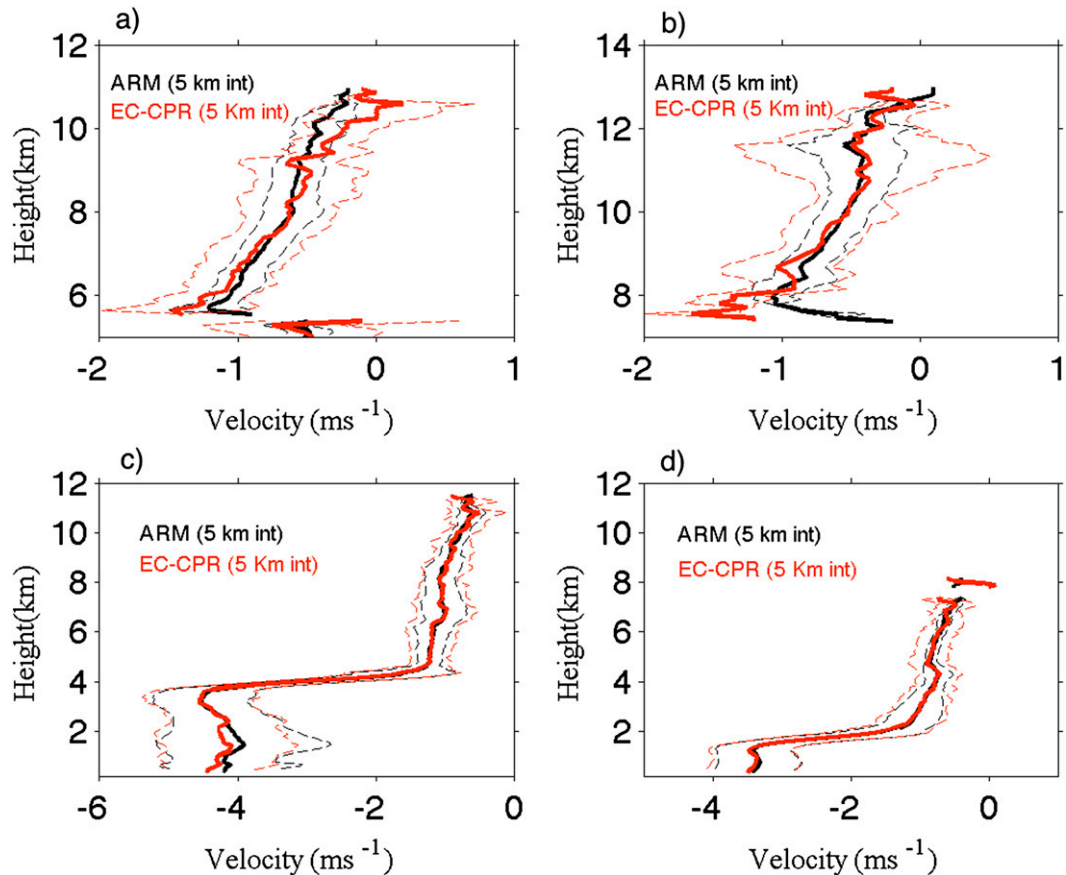
FIG. 13. Mean (solid lines) and standard deviation (dashed lines) of mean Doppler velocity (m s^{-1}) for four different ARM WACR cloud systems. Two cirrus cases: (a) 22 Nov 2004 (SGP) and (b) 7 Mar 2006 (TWP). Two stratiform precipitation cases: (c) 28 Aug 2006 (NIM) and (d) 1 Jun 2007 (FKB). The WACR Doppler velocity observations statistics are shown in black and the EC-CPR-simulated Doppler velocities statistics are shown in red. The integration length for both datasets is 5 km.

midlatitudes due to the gradual change in PRF from 6100 to 7500 Hz.

To investigate how often cloud and precipitation scenes satisfy the homogeneity condition, a large dataset of 94-GHz observations at various climatological regimes were analyzed to derive the statistics of reflectivity variability (ΔZ) for various along-track integrations. Overall, the statistics from all sites are remarkably similar. This increases the confidence in the climatology results and also raises interesting questions regarding controlling factors of cloud inhomogeneity as depicted by radar reflectivity measurements. On average, 66% of the observed changes in ΔZ are less than 3 dBZ for a horizontal length of 1000 m. The fraction of ΔZ changes less than 3 dB decreases significantly with horizontal distance in clouds and precipitation. The corresponding fractions for other horizontal lengths are: 55% for 2500 m and 48% for 5000 m. In particular, marine stratocumulus clouds sampled at Graciosa Island, Azores, exhibit very

large along-track variability, and it suggests that the along-track integration in drizzling stratus will often result in large Doppler biases due to nonuniform beam filling and reflectivity and velocities that are not representative of the integration length.

Finally, the CPR simulator is applied to a large number of cirrus and stratiform precipitation systems. Detailed results from two representative cirrus cloud and stratiform precipitation cases are discussed. In both cases, the simulated CPR Doppler velocities at low SNR conditions and near cloud boundaries were characterized by large uncertainties. In the case of the cirrus cloud simulation, along-track integration of 1000 m results in an average RMSD of 0.99 m s^{-1}. If an along-track integration of 5000 m and NUBF Doppler bias correction are applied, the RMSD reduces to 0.44 m s^{-1}. In the case of the large-scale precipitation, along-track integration of 5000 m can reduce the RMSD to 0.27 m s^{-1}. The CPR simulations demonstrated the importance of applying
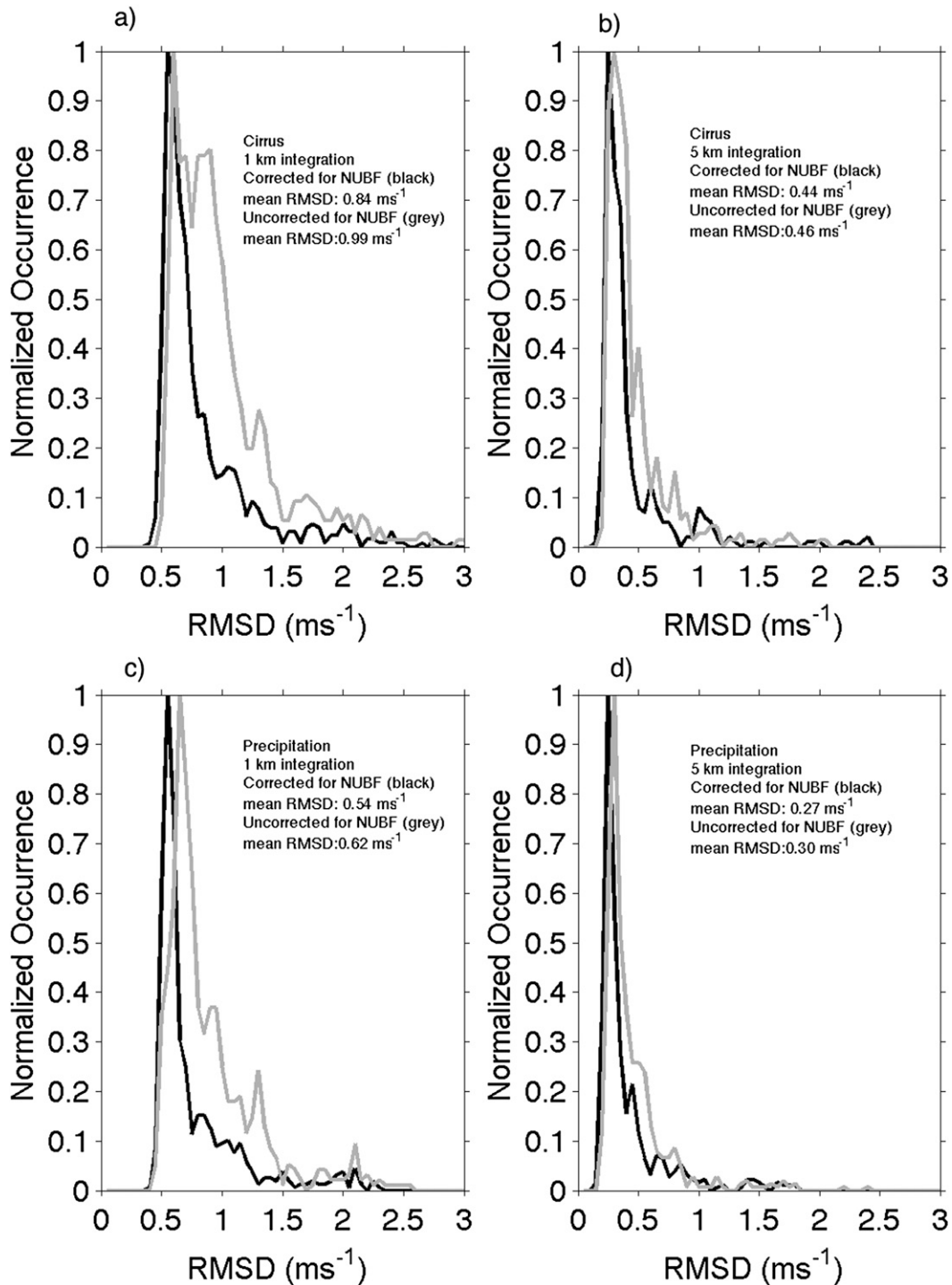
FIG. 14. Distributions of RMSD between ground-based (ARM) and simulated (CPR) for two integration lengths (left) 1000 and (right) 5000 m, and two different types of cloud systems: (a),(b) cirrus clouds and (c),(d) stratiform precipitation. The gray lines indicate the RMSD prior to NUBF corrections, and the solid black lines indicate the RMSD after the NUBF correction.

the NUBF Doppler velocity bias correction, especially for 1-km integration. Furthermore, the simulations indicated that despite that the selected areas are characterized by weak vertical motion, Doppler velocity folding is observed due to the high fall velocity of raindrops. A simple conditional algorithm was applied to unfold the simulated EC-CPR Doppler velocities. A more thorough analysis is needed for the development of an objective criterion that determines the along-track integration in order to reduce the CPR Doppler velocity variance but at the same time capable of accounting for the inhomogeneity of the integrated length.

In summary, there are several challenges in the Doppler-based retrievals from space that are not present in ground-based Doppler observations. The EC-CPR simulations suggest that the EC-CPR will be capable of detecting the main morphological Doppler velocity features from space (e.g., melting layer, increase of Doppler velocity with radar reflectivity). The estimated EC-CPR Doppler velocity RMSDs suggest that more research is needed in order to assess the potential for using the CPR Doppler velocities for retrieving the characteristic size of particle size distributions. This will be the topic of future research.

REFERENCES

Amayenc, P., J. Testud, and M. Marzoug, 1993: Proposal for a spaceborne dual-beam rain radar with Doppler capability. *J. Atmos. Oceanic Technol.,* **10,** 262–276.

Battaglia, A., S. Tanelli, S. Kobayashi, D. Zrnić, R. J. Hogan, and C. Simmer, 2010: Multiple-scattering in radar systems: A review. *J. Quant. Spectrosc. Radiat. Transfer,* **111,** 917–947.

——, T. Augustynek, S. Tanelli, and P. Kollias, 2011: Multiple scattering identification in spaceborne W-band radar measurements of deep convective cores. *J. Geophys. Res.,* **116,** D19201, doi:10.1029/2011JD016142.

Bechtold, P., E. Bazile, F. Guichard, P. Mascart, and E. Richard, 2001: A mass-flux convection scheme for regional and global models. *Quart. J. Roy. Meteor. Soc.,* **127,** 869–886.

Bony, S., and J.-L. Dufresne, 2005: Marine boundary layer clouds at the heart of tropical cloud feedback uncertainties in climate models. *Geophys. Res. Lett.,* **32,** L20806, doi:10.1029/2005GL023851.

Doviak, R. J., and D. S. Zrnić, 1993: *Doppler Radar and Weather Observations.* Academic Press, 562 pp.

EarthCARE, 2004: The six candidate Earth Explorer missions. ESA Reports for Mission Selection ESA SP-1279(1), 60 pp.

Horie, H., T. Kimura, K. Okada, Y. Ohno, K. Sato, and H. Kumagai, 2008: Study for external calibration method for cloud profiling radar on EarthCARE. *Sensors, Systems, and Next-Generation Satellites XII,* R. Meynart et al., Eds., International Society for Optical Engineering (SPIE Proceedings, Vol. 7106), 71060T, doi:10.1117/12.802335.

Joe, P., and Coauthors, 2010: The Polar Precipitation Measurement mission. *Proc. Sixth European Conf. on Radar in Meteorology and Hydrology,* Sibiu, Romania, ERAD. [Available online at http://www.erad2010.org/pdf/oral/tuesday/satellite/01_ERAD2010_Joe.pdf.]

Kobayashi, S., and H. Kumagai, 2003: Doppler velocity from sea surface on the spaceborne and airborne weather radars. *J. Atmos. Oceanic Technol.,* **20,** 372–381.

——, ——, and H. Kuroiwa, 2002: A proposal of pulse-pair Doppler operation on a spaceborne cloud-profiling radar in the W band. *J. Atmos. Oceanic Technol.,* **19,** 1294–1306.

Kollias, P., and B. A. Albrecht, 2005: Why the melting layer radar reflectivity is not bright at 94 GHz. *Geophys. Res. Lett.,* **32,** L24818, doi:10.1029/2005GL024074.

——, ——, R. Lhermitte, and A. Savtchenko, 2001: Radar observations of updrafts, downdrafts, and turbulence in fair-weather cumuli. *J. Atmos. Sci.,* **58,** 1750–1766.

——, E. E. Clothiaux, M. A. Miller, B. A. Albrecht, G. L. Stephens, and T. P. Ackerman, 2007a: Millimeter-wavelength radars: New frontier in atmospheric cloud and precipitation research. *Bull. Amer. Meteor. Soc.,* **88,** 1608–1624.

——, W. Szyrmer, I. Zawadzki, and P. Joe, 2007b: Considerations for spaceborne 94 GHz radar observations of precipitation. *Geophys. Res. Lett.,* **34,** L21803, doi:10.1029/2007GL031536.

Lhermitte, R., 1989: Satelliteborne millimeter wave Doppler radar. *Proc. URSI Commission F Open Symp.,* La Londe-les-Maures, France.

Manabe, S., and R. Strickler, 1964: Thermal equilibrium of the atmosphere with a convective adjustment. *J. Atmos. Sci.,* **21,** 361–385.

Matrosov, S., A. Battaglia, and P. Rodriguez, 2008: Effects of multiple scattering on attenuation-based retrievals of stratiform rainfall from CloudSat. *J. Atmos. Oceanic Technol.,* **25,** 2199–2208.

Meneghini, R., and T. Kozu, 1990: *Spaceborne Weather Radar.* Artech House, 212 pp.

Mitchell, D. L., P. Rasch, D. Ivanova, G. McFarquhar, and T. Nousiainen, 2008: Impact of small ice crystal assumptions on ice sedimentation rates in cirrus clouds and GCM simulations. *Geophys. Res. Lett.,* **35,** L09806, doi:10.1029/2008GL033552.

National Research Council, 2007: *Earth Science and Applications from Space: National Imperatives for the Next Decade and Beyond.* National Academies Press, 456 pp.

Ray, P. S., and C. Ziegler, 1977: De-aliasing first-moment Doppler estimates. *J. Appl. Meteor.,* **16,** 563–564.

Sanderson, B. M., C. Piani, W. J. Ingram, D. A. Stone, and M. R. Allen, 2008: Towards constraining climate sensitivity by linear analysis of feedback patterns in thousands of perturbed-physics GCM simulations. *Climate Dyn.,* **30,** 175–190.

Schutgens, N. A. J., 2008: Simulated Doppler radar observations of inhomogeneous clouds: Application to the EarthCARE space mission. *J. Atmos. Oceanic Technol.,* **25,** 26–42.

Serpetzoglou, E., B. Albrecht, P. Kollias, and C. W. Fairall, 2008: Boundary layer, cloud, and drizzle variability in the southeast Pacific stratocumulus regime. *J. Climate,* **21,** 6191–6214.

Sloss, P. W., and D. Atlas, 1968: Wind shear and reflectivity gradient effects on Doppler radar spectra. *J. Atmos. Sci.,* **25,** 1080–1089.

Stephens, G. L., and Coauthors, 2008: CloudSat mission: Performance and early science after the first year of operation. *J. Geophys. Res.,* **113,** D00A18, doi:10.1029/2008JD009982.

Stokes, G. M., and S. E. Schwartz, 1994: The Atmospheric Radiation Measurement (ARM) Program: Programmatic background and design of the Cloud and Radiation Test Bed. *Bull. Amer. Meteor. Soc.,* **75,** 1201–1222.

Tanelli, S., E. Im, S. L. Durden, L. Facheris, and D. Giuli, 2002a: The effects of nonuniform beam filling on vertical rainfall velocity measurements with a spaceborne Doppler radar. *J. Atmos. Oceanic Technol.,* **19,** 1019–1034.

——, ——, L. Facheris, and E. A. Smith, 2002b: DFT-based spectral moment estimators for spaceborne Doppler precipitation radar. *Microwave Remote Sensing of the Atmosphere and Environment III,* S. Tanelli et al. Eds., International Society for Optical Engineering (SPIE Proceedings, Vol. 4894), 218, doi:10.1117/12.467754.

——, ——, S. Kobayashi, R. Mascelloni, and L. Facheris, 2005: Spaceborne Doppler radar measurements of rainfall: Correction of errors induced by pointing uncertainties. *J. Atmos. Oceanic Technol.,* **22,** 1676–1690.

——, S. L. Durden, E. Im, K. S. Pak, D. Reinke, P. Partain, R. Marchand, and J. Haynes, 2008: CloudSat's Cloud Profiling Radar after two years in orbit: Performance, external calibration, and processing. *IEEE Trans. Geosci. Remote Sens.,* **46,** 3560–3573.

Testud J., P. H. Hildebrand, and W.-C. Lee, 1995: A procedure to correct airborne Doppler radar data for navigation errors using the echo returned from the earth's surface. *J. Atmos. Oceanic Technol.,* **12,** 800–819.

Tiedtke, M., 1989: A comprehensive mass flux scheme for cumulus parameterization in large-scale models. *Mon. Wea. Rev.,* **117,** 1779–1800.

Widener, K. B., and J. B. Mead, 2004: W-Band ARM cloud radar—Specifications and design. *Proc. 14th ARM Science Team Meeting,* Albuquerque, NM, ARM. [Available online at http://www.arm.gov/publications/proceedings/conf14/extended_abs/widener2-kb.pdf.]

Zrnić, D. S., 1975: Simulation of weatherlike Doppler spectra and signals. *J. Appl. Meteor.,* **14,** 619–620.

——, 1977: Spectral moments estimates from correlated pulse pairs. *IEEE Trans. Aerosp. Electron. Syst.,* **13,** 344–354.